The University of Osaka
Institutional Knowledge Archive

Title	Energetics of heterogeneous Mg {101¯2} deformation twinning migration using an atomistically informed phase-field model
Author(s)	Ishii, Akio
Citation	Computational Materials Science. 2020, 183, p. 109907
Version Type	VoR
URL	https://hdl.handle.net/11094/89305
rights	This is an open access article under the Creative Commons Attribution-NonCommercial-NoDerivatives 4.0 International license.
Note	

The University of Osaka Institutional Knowledge Archive : OUKA

https://ir.library.osaka-u.ac.jp/

The University of Osaka

Computational Materials Science 183 (2020) 109907

Contents lists available at ScienceDirect

Computational Materials Science

journal homepage: www.elsevier.com/locate/commatsci

Energetics of heterogeneous Mg {10$\bar{1}$2} deformation twinning migration using an atomistically informed phase-field model

Akio Ishii

[a] Department of Mechanical Science and Bioengineering, Osaka University, 1-3 Machikaneyama, Toyonaka, Osaka 560-8531, Japan

ARTICLE INFO

Keywords:
Phase-field model
Phase transformation
Molecular dynamics (MD)
Density functional theory
Deformation twinning

ABSTRACT

We have constructed an atomistically informed phase-field model for the quantitative energetic analysis of phase transformations. In our model, to describe the general phase transformation with a non-linear correlation between displacive and diffusive modes, we have defined two order parameters, γ and ϕ, which describe the lattice distortion (displacive mode) and shuffling (diffusive mode), respectively. Our method provides a way to introduce the energetics from atomistic simulations to the phase-field model, describes γ and ϕ in an atomic model, and derives phase-field parameters from the free energy calculated by atomistic simulation. As an application of our model, we used the energetics obtained from atomistic simulations using a density functional theory potential, and we calculated the free energy change during the heterogeneous {10$\bar{1}$2} twin migration of hexagonally close-packed (HCP) Mg, which can be considered as a lattice distortion and shuffling mixed phase transformation, by combining our phase-field model with the nudged elastic band method. The activation energy, and the critical nucleus size of the heterogeneous {10$\bar{1}$2} twin migration under a set stress were derived. The critical *c*-axis tensile stress (athermal stress), at which the activation energy becomes zero, is consistent with the experimental yield stress of {10$\bar{1}$2} for the twinning deformation of HCP Mg nanopillars in tensile tests. The critical nucleus size of the heterogeneous {10$\bar{1}$2} twin migration is on the range of nanometers under several hundred megapascals stress, which is consistent with the experimental observation of nanotwins.

1. Introduction

The phase-field method [1,2] is a promising mesoscale simulation method. In material science, the phase-field model is used for the analysis of the solidification or precipitate nucleation of metals [2], diffusion-less phase transformations (such as the martensitic deformation) [3,4], grain shape [5], and dislocation structure and displacement fields [6,7]. The phase-field model is a very powerful tool to predict the morphology of secondary phase nuclei in a parent phase, dendrite patterns [8–12], polycrystalline patterns [13], local stress patterns [3], and other phenomena [14,15]. Furthermore, the predicted patterns are in good agreement with those of experiment [2,16]. However, despite its success in morphological prediction, energetic analysis based on the phase-field model has been less successful [17]. For quantitative energetic analysis using the phase-field model, we must first calculate the energetics for use in the phase-field model, and the energetics must be calculated based on a reliable physical background. Atomistic simulations, i.e., molecular statics or dynamics using density functional theory (DFT) or empirical atomic potentials, can be used to calculate the energetics for the phase-field model. In particular, molecular statics or dynamics calculated using DFT potentials can provide non-empirical energetics for the phase-field model. Recently, the combination of the phase-field model with atomistic simulations has become a hot research topic, and many successful morphological analysis have been reported [18–23,7]. Generally, researchers have attempted to include atomistic simulation energetics in the phase-field model by utilizing the interface gradient parameter, γ-surface, or elastic constant information in the phase-field [18,19,24,25,20,7,21,22]. Despite these efforts, energetic analysis based on the phase-field model is still in the early stages, and a practical theoretical framework for the calculation of energetics using atomistic simulation is required to stimulate research in this area.

On the other hand, it is well known that general phase transformations have displacive and diffusive modes, and these two modes are nonlinearly correlated [26–28]. For solid–solid phase transformations such as deformation twinning or martensitic transformations, these correspond to lattice distortion and shuffling modes [29,30,27,31,32]. In this sense, the conventional phase-field model, which describes the phase transformation with *only* a single order parameter, is not sufficiently accurate to express the phase transformation because it cannot express the non-linear correlation between lattice distortion and shuffling. This deficiency has motivated researchers to discuss the non-linearity between the eigenstrain (transformation strain) and the order

E-mail address: ishii@me.es.osaka-u.ac.jp.

https://doi.org/10.1016/j.commatsci.2020.109907
Received 26 May 2020; Received in revised form 24 June 2020; Accepted 25 June 2020
Available online 10 July 2020
0927-0256/ © 2020 The Author. Published by Elsevier B.V. This is an open access article under the CC BY-NC-ND license (http://creativecommons.org/licenses/BY-NC-ND/4.0/).

parameter [33]. Although variant phases, orientation change and nonlinear elasticity of phase transformation are considered in present phase-field model [34–37], we think there is no phase-field framework to distinguish the displacive and diffusive modes of phase transformation. For this, we need to correlate the order parameter of phase-field model with atomic structure change because the shuffling is caused by local cooperative atomic displacement [27].

In this study, we constructed an atomistically informed phase-field model to analyze the phase transformation quantitatively. In our model, two order parameters, γ and ϕ, are defined, and these parameters describe the lattice distortion and shuffling, respectively, required to express the phase transformation. All information required for the phase-field dynamics, including the energetics of the γ and ϕ correlation and phase-field parameters for uniform and heterogeneous phase transformation, are obtained using atomistic simulation. Here, a theoretical framework to calculate this energetic information from atomistic simulations for use in the phase-field model is provided: in particular, a description of γ and ϕ in the atomic model and a way to derive phase-field parameters from the free energy calculated by atomistic simulation. As an application of our model, we used the free energy calculated using molecular statics calculations with a DFT potential, and we calculated the free energy change during the heterogeneous $\{10\bar{1}2\}$ twin migration of hexagonally close-packed (HCP) Mg, which can be considered as a lattice distortion (displacive) and shuffling (diffusive) mixed phase transformation [27,38]. From the free energy change, the activation energy, critical nucleus size under certain stress conditions, and critical stress of the heterogeneous $\{10\bar{1}2\}$ twin migration were obtained and are discussed from an energetic perspective.

2. Atomistically informed phase-field model

2.1. Basic theory

To obtain the energetics from atomistic simulation for use in the phase-field model, we must connect the discrete atomic model with the continuous phase-field model. As shown in Fig. 1, we start with an atomic supercell, Ω, which includes the parent, secondary phase, and middle state of a certain phase transformation. The associated lattice distortion and shuffling and the phase transformation can be described well by a lattice unit (we call it the phase transformation unit here) in this supercell. Next, the phase transformation units in the atomic supercell are treated as grid points in the phase-field model; i.e., the local atomic structure of the phase transformation unit at position $\boldsymbol{x}$ (e.g., suppose $\boldsymbol{x}$ is the center of the phase-field unit) is related to lattice distortion order parameter $\gamma(\boldsymbol{x})(0 \leqslant \gamma \leqslant 1)$ and shuffling order parameter $\phi(\boldsymbol{x})(0 \leqslant \phi \leqslant 1)$ at grid point $\boldsymbol{x}$ in the phase-field model using the cell shape change and internal atomic displacement [27] of the phase transformation unit.

Moreover, we can calculate the total free energy of the whole Ω supercell, $G_{\mathrm{AS}}(\bar{\sigma}, \overline{T})$, under average stress $\bar{\sigma}$ at temperature $\overline{T}$ ($n\sigma T$ ensemble) using atomistic simulation. The subscript "AS" indicates that the total free energy is obtained from atomistic simulation. In the phase-field model, this total free energy G_{AS} is described as the integral of the local free energy $g(\boldsymbol{x})$ over the whole Ω system,

$$G_{\mathrm{AS}}\left(\bar{\sigma}, \overline{T}\right) - G^0_{\mathrm{AS}}\left(\bar{\sigma}, \overline{T}\right) = \int_{\Omega} g(\boldsymbol{x}) d\boldsymbol{x}. \tag{1}$$

Here, $G^0_{\mathrm{AS}}(\bar{\sigma}, \overline{T})$ is the reference free energy. Referring to Cahn and Hilliard's theory [39], we can describe g as a functional of order parameters $\gamma(\boldsymbol{x})$ and $\phi(\boldsymbol{x})$,

$$g(\boldsymbol{x}) = g(\gamma(\boldsymbol{x}), \phi(\boldsymbol{x}), \nabla\gamma(\boldsymbol{x}), \nabla\phi(\boldsymbol{x}), \nabla^2\gamma(\boldsymbol{x}), \nabla^2\phi(\boldsymbol{x}), ..., \bar{\sigma}, \overline{T}). \tag{2}$$

The γ and ϕ terms describe the intrinsic energy change of the phase transformation unit arising from the lattice distortion and shuffling, respectively. The gradient terms, $\nabla\gamma$, $\nabla^2\gamma$, ...($\nabla\phi$, $\nabla^2\phi$, ...), describe the heterogeneous interaction between the phase transformation units (unit–unit interaction) caused by local lattice distortion (shuffling). In other words, the gradient terms $\nabla\gamma$, $\nabla^2\gamma$, ...($\nabla\phi$, $\nabla^2\phi$, ...) describe the elastic (chemical) unit–unit interactions. Additionally, we regard $g(\boldsymbol{x})$ as a function of $\bar{\sigma}$ and $\overline{T}$ for convenience to provide $G_{\mathrm{AS}}(\bar{\sigma}, \overline{T})$ of the $n\sigma T$ ensemble atomistic simulation. Note that our goal is different from that of the multi-phase-field model [40,41], even though we have two order parameters in our model. Although the order parameters in the multi-phase-field model are used to express the variation in the phase or orientation in the system [36,37], our order parameters are used to obtained a more exact expression of a single phase transformation.

In the next step, g is approximately divided into the elastic unit–unit interaction energy, i.e., the gradient terms of γ: $\nabla\gamma$, $\nabla^2\gamma$, ..., and other terms, such as g_{elast} and $\tilde{g}$,

$$g(\gamma, \phi, \nabla\gamma, \nabla\phi, \nabla^2\gamma, \nabla^2\phi, ..., \bar{\sigma}, \overline{T}) \approx \tilde{g}(\gamma, \phi, \nabla\phi, \nabla^2\phi, ..., \bar{\sigma}, \overline{T}) + g_{\mathrm{elast}}(\nabla\gamma, \nabla^2\gamma, ..., \bar{\sigma}, \overline{T}). \tag{3}$$

The eigenstrain (or transformation strain [42,43,33]) induced by the phase transformation has a linear relationship to $\gamma(\boldsymbol{x})$, thus $\gamma\epsilon$. ϵ is the eigenstrain induced by the complete phase transformation. Referring to the micromechanics of Mura et al. [44], g_{elast} is given by

$$g_{\mathrm{elast}}\left(\nabla\gamma, \nabla^2\gamma, ..., \bar{\sigma}, \overline{T}\right) = \frac{1}{2}\left\{\left(\bar{\sigma} + \Delta\sigma(\boldsymbol{x})\right) : \left(\bar{\varepsilon} + \Delta\varepsilon(\boldsymbol{x}) - \gamma\epsilon\right)\right\} - \bar{\sigma} : \bar{\varepsilon}\Big\}. \tag{4}$$

$\bar{\varepsilon}$ is average strain caused by $\bar{\sigma}$. $\Delta\sigma(\boldsymbol{x})$ and $\Delta\varepsilon(\boldsymbol{x})$ are local stress and local strain deviations, which describe the unit–unit elastic interaction. Thus, the local stress can be given by $\sigma(\boldsymbol{x}) = \bar{\sigma} + \Delta\sigma(\boldsymbol{x})$ and the local strain by $\varepsilon(\boldsymbol{x}) = \bar{\varepsilon} + \Delta\varepsilon(\boldsymbol{x})$. The $-\bar{\sigma} : \bar{\varepsilon}$ term eliminates the elastic energy caused by uniform deformation, which is included in the $\tilde{g}$ term. For finite temperature analysis, a temperature term is included in eigenstrain term as a thermal strain effect, $\epsilon = \epsilon(\overline{T})$. Once the eigenstrain has been determined, the local stress and strain can be calculated by solving Poisson's equation using the Fourier transform of eigenstrain [44,42]. Although it seems that the eigenstrain caused by lattice distortion is linearly related to γ as $\gamma\epsilon$ in Eq. (4) (as discussed later) because the order parameter γ is nonlinearly correlated with the shuffling order parameter ϕ based on the atomistically informed $\gamma - \phi$ free energy map, non-linear correlation between the lattice distortion and shuffling [33] can be achieved in our model.

Again, referring to Cahn and Hilliard's theory [39], we ignore the high-order gradient terms ϕ larger than 3 in $\tilde{g}$: $\tilde{g}(\gamma, \phi, \nabla\phi, \nabla^2\phi, ..., \bar{\sigma}, \overline{T}) \approx \tilde{g}(\gamma, \phi, \nabla\phi, \nabla^2\phi, \bar{\sigma}, \overline{T})$, and divide $\tilde{g}$ into the intrinsic term $\tilde{g}_{\mathrm{int}}(\gamma, \phi, \bar{\sigma}, \overline{T}) \equiv \tilde{g}(\gamma, \phi, 0, 0, \bar{\sigma}, \overline{T})$ and heterogeneous unit–unit shuffling interaction terms by using McLaughlin's first-order expansion of $\nabla\phi$ and $\nabla^2\phi$:

$$\tilde{g}\left(\gamma, \phi, \nabla\phi, \nabla^2\phi, \bar{\sigma}, \overline{T}\right) \approx \tilde{g}_{\mathrm{int}}\left(\gamma, \phi, \bar{\sigma}, \overline{T}\right) + \sum_i L^{\mathrm{I}}_i\left(\gamma, \phi, \nabla^2\phi, \bar{\sigma}, \overline{T}\right)\left(\frac{\partial\phi}{\partial x_i}\right) + \sum_{ij} L^{\mathrm{II}}_{ij}\left(\gamma, \phi, \nabla\phi, \bar{\sigma}, \overline{T}\right)\left[\left(\frac{\partial\phi}{\partial x_i}\right)\left(\frac{\partial\phi}{\partial x_j}\right)\right],$$

$$L^{\mathrm{I}}_i\left(\gamma, \phi, \nabla^2\phi, \bar{\sigma}, \overline{T}\right) = \left[\frac{\partial g}{\partial\left(\frac{\partial\phi}{\partial x_i}\right)}\right]_{\nabla\phi=0}$$

$$L^{\mathrm{II}}_{ij}\left(\gamma, \phi, \nabla\phi, \bar{\sigma}, \overline{T}\right) = \left[\frac{\partial^2 g}{\partial\left(\frac{\partial\phi}{\partial x_i}\right)\left(\frac{\partial\phi}{\partial x_j}\right)}\right]_{\nabla^2\phi=0}. \tag{5}$$

We use the subscripts i and j to denote the substitution of the x, y, and z components for the variable x_i. Following the conventional phase-field model approximation, $L^{\mathrm{I}}_i(\gamma, \phi, \nabla^2\phi, \bar{\sigma}, \overline{T}) \approx 0$ and $L^{\mathrm{II}}_{ij}(\gamma, \phi, \nabla\phi, \bar{\sigma}, \overline{T}) \approx L^{\mathrm{II}}_{ij}(\bar{\sigma}, \overline{T})$ [39,1]. Finally, as phase-field

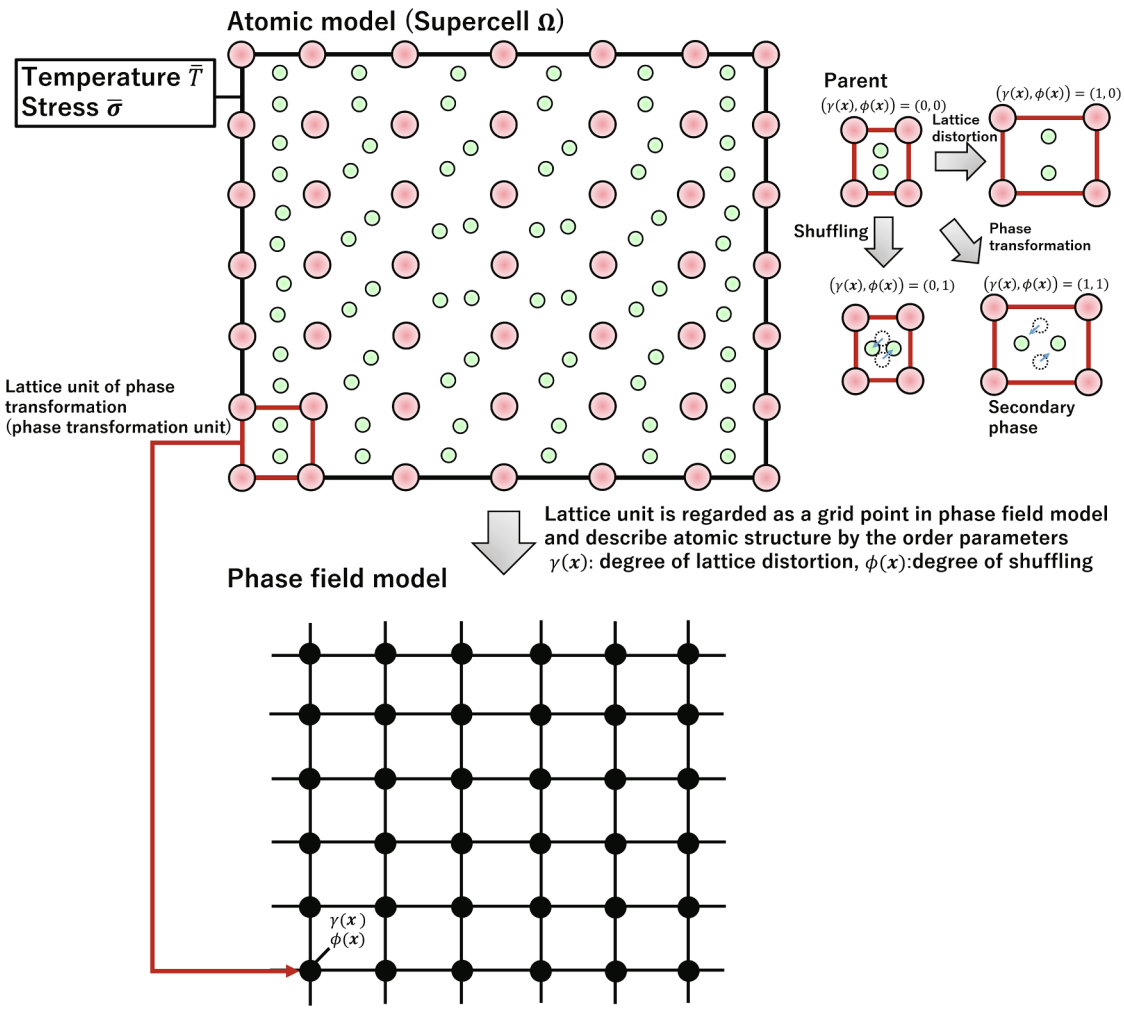

Fig. 1. Schematic of the atomistically informed phase-field model. The continuous phase-field model is connected to a discrete atomic supercell, Ω. Atomic supercell Ω, which includes parent and secondary phases and a middle state of a virtual phase transformation of the 2-dimensional atomic structure with red and green atom species, is replaced by the phase-field model with two order parameters: $\gamma(x)$ and $\phi(x)$. The order parameters γ and ϕ at each grid point in the phase-field model are described using the change in cell shape (i.e., the atomic displacement of the red atom) and internal atomic displacement (i.e., the atomic displacement of the green atom) of a lattice unit (phase transformation unit) during the phase transformation, which correspond to the lattice distortion and shuffling, respectively. The black frame in the atomic structure represents the periodic boundary. (For interpretation of the references to colour in this figure legend, the reader is referred to the web version of this article.)

parameters, only $\tilde{g}_{\mathrm{int}}$ and are required using the above approximation. In the next section, we show how to describe order parameters γ and ϕ in a given atomic phase transformation unit and how to calculate $\tilde{g}_{\mathrm{int}}$ and L_{ij}^{II} from the atomistic simulation data using γ and ϕ based on the above theory.

2.2. Description of order parameters: Lattice distortion γ and shuffling ϕ

In Fig. 2, we show a virtual phase transformation of 2-dimensional atomic structure, including red and green atoms, from the parent to secondary phase, as already shown in Fig. 1. The red frame in the figure delimits the phase transformation unit and includes one red (atom A) and two green (atoms B and C) atoms. In addition, $\boldsymbol{r}_{\mathrm{A}}$, $\boldsymbol{r}_{\mathrm{B}}$, and $\boldsymbol{r}_{\mathrm{C}}$ denote the atomic positions of atoms A, B, and C in Cartesian coordinates, and $\boldsymbol{h}_i$ is the edge vector of the unit and can be described using the position of atom $\mathrm{A_i}$, i.e., $\boldsymbol{r}_{\mathrm{A_i}}$; this atom belongs to the adjacent unit along the $\boldsymbol{x}_i$-direction as $\boldsymbol{h}_i = \boldsymbol{r}_{\mathrm{A}} - \boldsymbol{r}_{\mathrm{A_i}}$. Note $\boldsymbol{r}_{\mathrm{A_i}}$ is crystallographically equivalent to $\boldsymbol{r}_{\mathrm{A}}$ if the phase transformation is uniform in whole system. The superscripts "p", "2nd", and the tilde on these variables in Fig. 2 indicate that they belong to the parent phase, secondary phase, and middle state atomic structure of the phase transformation, respectively. The red and blue arrows indicate the change in cell shape and internal atomic displacement, which correspond to the lattice distortion and shuffling, respectively, during the phase transformation.

Now, we explain how to describe the order parameters ($\tilde{\gamma}$ and $\tilde{\phi}$) of the middle state from the atomic structure information of the middle state, parent phase, and secondary phase. To express the lattice distortion (red arrows show the cell shape change in Fig. 2), using cell matrix $\boldsymbol{H} \equiv [\boldsymbol{h}_1 \boldsymbol{h}_2]$, we describe the deformation gradient tensor $\boldsymbol{J}$ and eigenstrain ϵ of the phase transformation unit caused by the phase transformation as [45]

$$(\boldsymbol{J})^T = \boldsymbol{H}(\boldsymbol{H}^{\mathrm{p}})^{-1}, \quad \epsilon = \frac{1}{2}(\boldsymbol{J}^T\boldsymbol{J} - \boldsymbol{I}). \tag{6}$$

Then, we describe $\tilde{\gamma}$ as

$$\tilde{\gamma} = \frac{\tilde{\epsilon} : \epsilon^{2\mathrm{nd}}}{\epsilon^{2\mathrm{nd}} : \epsilon^{2\mathrm{nd}}}. \tag{7}$$

Here, $\tilde{\epsilon}$ and $\epsilon^{\mathbf{2nd}}$ correspond to the eigenstrains caused by the lattice distortion of middle state and secondary phase structures, respectively. The volume of the phase transformation unit is described as $V_0 = \mathrm{tr}(\boldsymbol{H}^{\mathrm{p}})$. On the other hand, to express the shuffling (blue arrows in

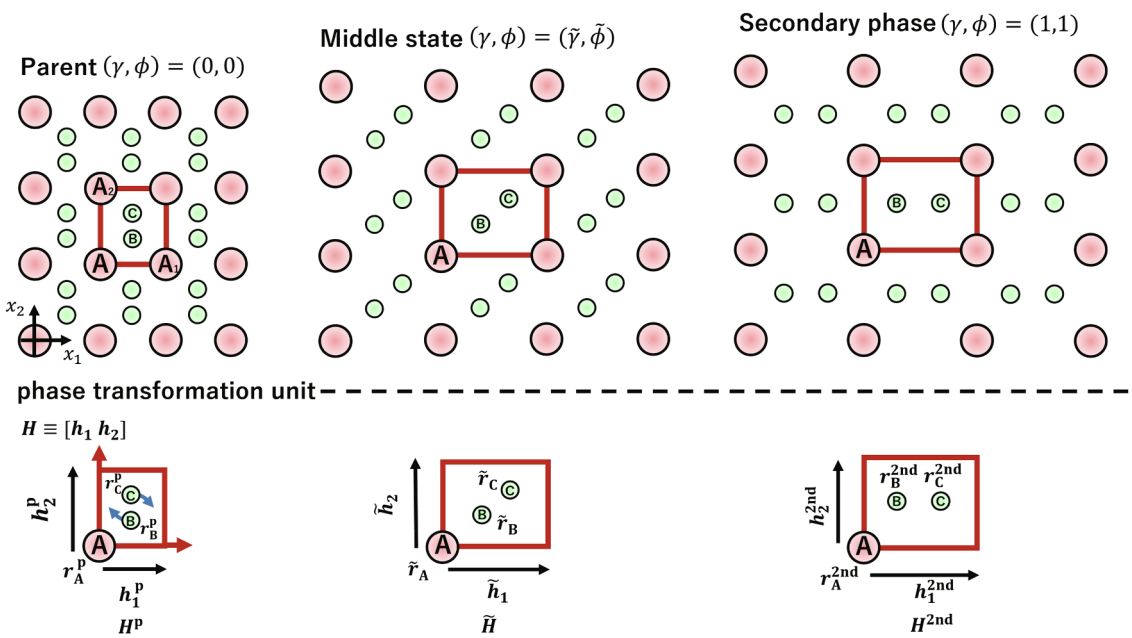

Fig. 2. Virtual phase transformation of the 2-dimensional atomic structure with red and green atom species. The red frame shows the phase transformation unit. Red and blue arrows indicate the cell shape change and internal atomic displacement, which correspond to the lattice distortion and shuffling, respectively, during the phase transformation. (For interpretation of the references to colour in this figure legend, the reader is referred to the web version of this article.)

Fig. 2), we describe internal coordinate [27] $\boldsymbol{s}$ as $\boldsymbol{s} = \boldsymbol{H}^{-1}\boldsymbol{r}$. In addition, using $\boldsymbol{S} \equiv [\boldsymbol{s}_{\mathrm{A}};\boldsymbol{s}_{\mathrm{B}};\boldsymbol{s}_{\mathrm{C}}]$,

$$\tilde{\phi} = \frac{(\tilde{\boldsymbol{S}} - \boldsymbol{S}^{\mathrm{p}})^T(\boldsymbol{S}^{\mathrm{2nd}} - \boldsymbol{S}^{\mathrm{p}})}{(\boldsymbol{S}^{\mathrm{2nd}} - \boldsymbol{S}^{\mathrm{p}})^T(\boldsymbol{S}^{\mathrm{2nd}} - \boldsymbol{S}^{\mathrm{p}})}. \tag{8}$$

Here, $\boldsymbol{s}_{\mathrm{A}}$, $\boldsymbol{s}_{\mathrm{B}}$, and $\boldsymbol{s}_{\mathrm{C}}$ are the internal coordinates of atoms A, B, and C, respectively. For the conventional 3-dimensional phase transformation unit including 1, ...,n atoms, the coordinates of a certain atom is used to calculate $\boldsymbol{H} = [\boldsymbol{h}_1\boldsymbol{h}_2\boldsymbol{h}_3]$, and the coordinates of all atoms are used to calculate the 3n-dimensional internal coordinate $\boldsymbol{S} \equiv [\boldsymbol{s}_1;\boldsymbol{s}_2;\boldsymbol{s}_3;...;\boldsymbol{s}_n]$ to derive $\tilde{\phi}$. Additionally, for the finite temperature analysis, atom coordinate $\boldsymbol{r}$ is replaced by time-averaged atom position $\langle \boldsymbol{r} \rangle$ at thermal equilibrium. The order parameters are described as averaged atomic positions, and the thermal effect is included in the eigenstrain $\epsilon^{\mathrm{2nd}}(\overline{T})$ in Eq. (4) by using finite temperature $\boldsymbol{H}(\overline{T})$. Note, as a phase transformation unit, the best choice is the minimum unit cell which can describe shuffling atomic displacement of the phase transformation, otherwise the gradient term may appear inside the phase transformation unit itself, leading the wrong energetics to phase-field model.

2.3. Atomistically informed phase-field parameters $\tilde{g}_{\mathrm{int}}$ and L_{ij}^{II}

Utilizing the above definition of γ and ϕ in the atomic system, conventional atomistic simulations using DFT or empirical potentials provide the quantitative total free energy, G_{AS}, of the system with a clear expression of the $\gamma(\boldsymbol{x})$ and $\phi(\boldsymbol{x})$ distribution for use in the phase-field model. Next, a single phase transformation unit, in which the ordering parameters are $\tilde{\gamma}$ and $\tilde{\phi}$, are used as a supercell to provide $\tilde{g}_{\mathrm{int}}(\tilde{\gamma}, \tilde{\phi}, \bar{\sigma}, \overline{T})$. Using this supercell, we can estimate the free energy change atomistically during uniform phase transformation without any unit–unit interactions. As shown in Fig. 3, discrete $\tilde{g}_{\mathrm{int}}$ can be obtained using the free energy $(G_{\mathrm{AS}}^{\mathrm{uni}}(\tilde{\gamma}, \tilde{\phi}, \bar{\sigma}, \overline{T}))$ provided from the molecular statics (zero temperature) or dynamics (finite temperature) constrained γ and ϕ of the supercell [27],

$$\tilde{g}_{\mathrm{int}}(\tilde{\gamma}, \tilde{\phi}, \bar{\sigma}, \overline{T}) = G_{\mathrm{AS}}^{\mathrm{uni}}(\tilde{\gamma}, \tilde{\phi}, \bar{\sigma}, \overline{T}) - G_{\mathrm{AS}}^{\mathrm{uni}}(0, 0, 0, 0). \tag{9}$$

Once discrete $\tilde{g}_{\mathrm{int}}$ has been calculated, the whole $\tilde{g}_{\mathrm{int}}$ map can be achieved using an interpolation method. In this way, the order parameters γ and ϕ are correlated nonlinearly by the $\tilde{g}_{\mathrm{int}}$ map obtained via atomistic simulation; this means that the physical meaning of the non-linear relationship between the lattice distortion and shuffling is guaranteed by the atomistic simulation. This is a distinct advantage of our model compared to others and provides an answer to the recent discussion about the relationship between the order parameter and the eigenstrain [33].

To derive L_{ij}^{II}, supercells including $\frac{\partial\phi}{\partial x_i}\frac{\partial\phi}{\partial x_j}$ terms are necessary. Although there are many supercell candidates that have $\frac{\partial\phi}{\partial x_i}\frac{\partial\phi}{\partial x_j}$ terms, for simplicity, we use the following two types of supercell to derive L_{ii}^{II} and $L_{ij}^{\mathrm{II}}(i \neq j)$ individually. For the calculation of L_{ii}^{II}, we use supercells that can describe the x_i interface individually; i.e., a supercell Ω_{ii} that has parent and secondary phases and *only* an x_i interface plane, as shown in Fig. 4(a). This means that supercell Ω_{ii} includes a $\frac{\partial^2\phi}{\partial x_i^2}$ term but no $\frac{\partial\phi}{\partial x_i}\frac{\partial\phi}{\partial x_i}\left(i \neq j\right)$ term. Using the free energy $(G_{\mathrm{AS}}^{ii}(\bar{\sigma}, \overline{T}))$ provided by atomistic simulation with this heterogeneous supercell, which contains x_i interface planes, and Eqs. (1), (3), and (5)

$$\begin{aligned} L_{ii}^{\mathrm{II}}\left(\bar{\sigma}, \overline{T}\right) \approx \frac{1}{\int_{\Omega_{ii}} \frac{\partial^2\phi}{\partial x_i^2} d\boldsymbol{x}} \Bigg\{ & (G_{\mathrm{AS}}^{ii}(\bar{\sigma}, \overline{T}) - M_{ii} G_{\mathrm{AS}}^{\mathrm{uni}}(0, 0, 0, 0)) \\ & - \int_{\Omega_{ii}} g_{\mathrm{elast}}\left(\frac{\partial\gamma}{\partial x_i}, \frac{\partial^2\gamma}{\partial x_i^2}, ..., \bar{\sigma}, \overline{T}\right) d\boldsymbol{x} \\ & - \int_{\Omega_{ii}} \tilde{g}_{\mathrm{int}}\left(\gamma, \phi, \bar{\sigma}, \overline{T}\right) d\boldsymbol{x} \Bigg\}. \end{aligned} \tag{10}$$

M_{ii} is the number of phase transformation units contained in supercell Ω_{ii}. Here, $\int_{\Omega_{ii}} \frac{\partial^2\phi}{\partial x_i^2} d\boldsymbol{x}$ can be estimated from the $\phi(\boldsymbol{x})$ distribution. The G_{AS}^{ii}, $G_{\mathrm{AS}}^{\mathrm{uni}}$, and $\tilde{g}_{\mathrm{int}}$ terms are obtained from atomistic simulation, and the g_{elast} term can be estimated by micromechanics using Eq. (4). The integral of these terms can also be calculated using the $\gamma(\boldsymbol{x})$ and $\phi(\boldsymbol{x})$ distribution in the supercell. Once L_{ii}^{II} has been obtained, we can calculate L_{ij}^{II} using the $\Omega_{ij}(i \neq j)$ supercell, which has parent and secondary phases, x_i and $x_j(i \neq j)$ interface planes, and $i - j$ interface corners, as shown in Fig. 4(b). This means that supercell Ω_{ij} includes

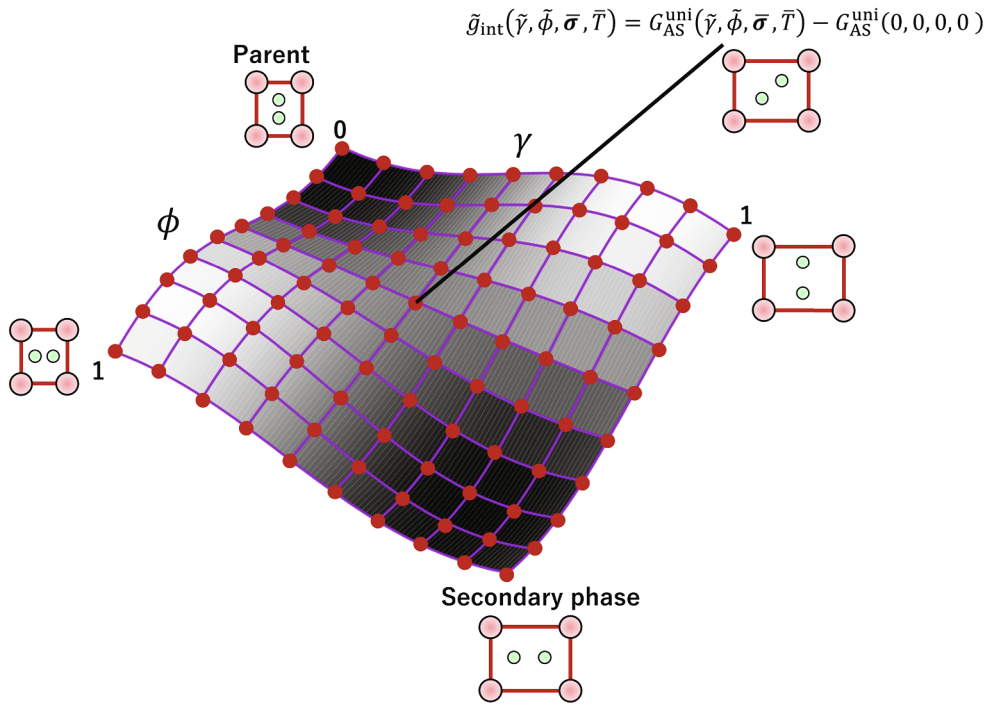

Fig. 3. Schematic of atomistically informed $\tilde{g}_{\mathrm{int}}$. Atomistic simulation using a single phase transformation unit as a supercell provides discrete $\tilde{g}_{\mathrm{int}}(\gamma, \phi, \bar{\sigma}, \bar{T})$ (red dots). The whole $\tilde{g}_{\mathrm{int}}$ map can be achieved by interpolation. (For interpretation of the references to colour in this figure legend, the reader is referred to the web version of this article.)

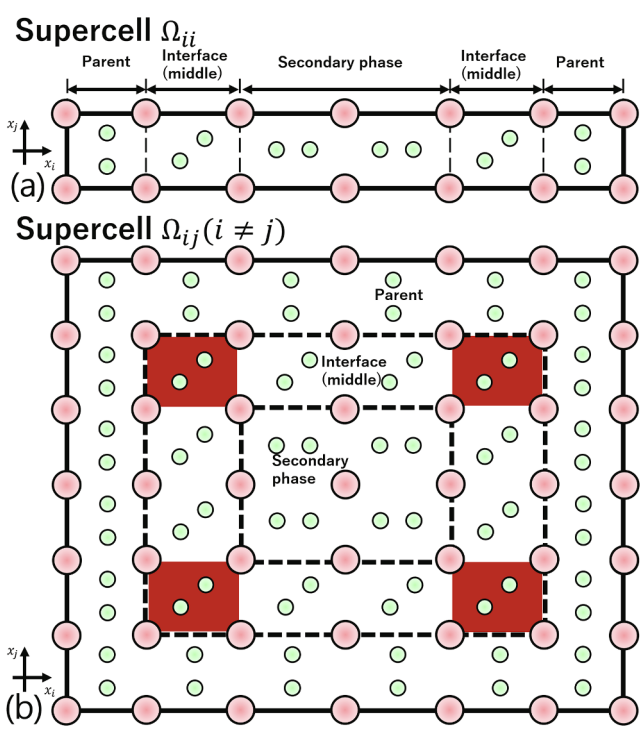

Fig. 4. Supercells (a) Ω_{ii} and (b) $\Omega_{ij}(i \neq j)$, which contain the parent and secondary phases and (a) x_i interface planes and (b) x_i and $x_j(j \neq i)$ interface planes and corners, respectively. The black frame represents the periodic boundary. Red regions in (b) are the phase-field units at the corners. (For interpretation of the references to colour in this figure legend, the reader is referred to the web version of this article.)

both a $\frac{\partial^2\phi}{\partial x_i^2}$ term (interface edge) and $\frac{\partial\phi}{\partial x_i}\frac{\partial\phi}{\partial x_j}\left(i \neq j\right)$ term (interface corner). Again, using the free energy ($G_{\mathrm{AS}}^{ij}(\bar{\sigma}, \bar{T})(i \neq j)$) of the system provided by atomistic simulation,

$$L_{ij}^{\mathrm{II}}\left(\bar{\boldsymbol{\sigma}}, \bar{T}\right) \approx \frac{1}{\int_{\Omega_{ij}} \frac{\partial\phi}{\partial x_i}\frac{\partial\phi}{\partial x_j} d\boldsymbol{x}} \left\{ \left(G_{\mathrm{AS}}^{ij}(\bar{\boldsymbol{\sigma}}, \bar{T}) - M_{ij} G_{\mathrm{AS}}^{\mathrm{uni}}\left(0, 0, 0, 0\right)\right) - \int_{\Omega_{ij}} g_{\mathrm{elast}}\left(\frac{\partial\gamma}{\partial x_i}, \frac{\partial\gamma}{\partial x_j}, \frac{\partial^2\gamma}{\partial x_i^2}, \frac{\partial^2\gamma}{\partial x_j^2}, \frac{\partial\gamma}{\partial x_i}\frac{\partial\gamma}{\partial x_j}, \ldots, \bar{\boldsymbol{\sigma}}, \bar{T}\right) d\boldsymbol{x} - \int_{\Omega_{ij}} \tilde{g}_{\mathrm{int}}\left(\gamma, \phi, \bar{\sigma}, \bar{T}\right) d\boldsymbol{x} - \int_{\Omega_{ij}} \left(L_{ii}^{\mathrm{II}} \frac{\partial^2\phi}{\partial x_i^2} + L_{jj}^{\mathrm{II}} \frac{\partial^2\phi}{\partial x_j^2}\right) d\boldsymbol{x} \right\}. \tag{11}$$

Here, $M_{ij}(i \neq j)$ is the number of phase transformation units contained in the supercell Ω_{ij}. Note that for the finite temperature analysis, the free energy from atomistic simulation (G_{AS}) is replaced by the time-averaged free energy, i.e., $\langle G_{\mathrm{AS}} \rangle$, at thermal equilibrium.

3. Application: Energetics of heterogeneous Mg $\{10\bar{1}2\}$ twin migration

3.1. Background

As a practical application of our model, we calculated the activation energy and the critical nucleus size of $\{10\bar{1}2\}$ twin migration of HCP Mg under defined stress conditions using DFT molecular statics information. The $\{10\bar{1}2\}$ deformation twinning is one of the most frequently observed plastic deformations of HCP metals [46]. In particular, for HCP Mg, this deformation is the dominant plastic deformation on the application of *c*-axis ([0001]-direction) tension [47,48]. Because $\{10\bar{1}2\}$ deformation twinning is a phase transformation involving both lattice distortion and shuffling [30,49,50,27], molecular dynamics and statics simulations using empirical or DFT atomic potentials are popular, and, to date, the atomic morphologies of $\{10\bar{1}2\}$ deformation twinning under

many situations have been well studied [51–53]. However, energetic studies of $\{10\bar{1}2\}$ deformation twinning remain insufficient. Although there have been several studies of the activation energy of uniform $\{10\bar{1}2\}$ twinning deformations [49,27,54] and twinning boundary energies [55,56] using DFT potentials, as well as the activation energy of 2-dimensional twin migration [57,58] using empirical potentials, the study of the energetics of realistic 3-dimensional heterogeneous $\{10\bar{1}2\}$ twinning nucleation or migration based on DFT potentials has not been carried out because of the high calculation cost of atomistic simulations. Nevertheless, recently, heterogeneous Mg $\{10\bar{1}2\}$ twin migration has been studied using a combined model of molecular statics and conventional phase-field models, in which the interface energy (gradient parameter) in the phase-field is provided by molecular statics [22,21], but the activation energy and the critical nucleus size have not yet been discussed.

3.2. DFT molecular statics simulation of $\{10\bar{1}2\}$ deformation twinning to obtain phase-field parameters

In Fig. 5, we show the change in the atomic structure during the uniform $\{10\bar{1}2\}$ twinning deformation of HCP Mg. The Cartesian coordinate axes $\boldsymbol{x_1}$, $\boldsymbol{x_2}$, and $\boldsymbol{x_3}$ are parallel to $[10\bar{1}0]$, $[0001]$, and $[\bar{1}2\bar{1}0]$, respectively. The phase transformation unit, the minimum unit of the $\{10\bar{1}2\}$ twining deformation, includes four atoms: A, B, C, and D, respectively [49,27]. Lattice distortion is described using atom A and A_i, and atoms B, C, and D need shuffling for this transformation. After the twinning deformation, the phase transformation unit is rotated 86° around the center of the unit [59], and an eigenstrain of approximately $\epsilon_{11}^{2nd} = -0.062$, $\epsilon_{22}^{2nd} = 0.062$ is induced. For the $\tilde{g}_{int}$ calculation, we used the supercell model of this unit. G_{AS}^{uni} was calculated at 196 middle points in the range of $0 < \gamma < 1$, $0 < \phi < 1$ using molecular statics ionic structure relaxation constraining γ and ϕ under set stress conditions, and the full space continuous $\tilde{g}_{int}(\gamma, \phi)$ was interpolated using a spline function.

For the $L_{11}^{II}(L_{33}^{II})$ calculation, as in Fig. 6, we prepared linear supercell $\Omega_{11}^{twin}(\Omega_{11}^{twin})$ with six original (parent) ($\gamma = \phi = 0$) and six twin ($\gamma = \phi = 1$) units along the $\boldsymbol{x_1}(\boldsymbol{x_3})$-direction containing 48 Mg atoms and carried out molecular statics ionic structure relaxation under zero stress conditions to obtain $G_{AS}^{11}(0, 0)$ ($G_{AS}^{33}(0, 0)$) and $\phi(\boldsymbol{x})$ and $\gamma(\boldsymbol{x})$ distribution. Note $L_{22}^{II} = L_{11}^{II}$ because basal-prismatic (BP) and prismatic-basal (PB) boundaries are crystallographically equivalent [55]. The middle state atomic structure around the twin boundary, as for the interface shown in Fig. 4, is automatically obtained during this structural relaxation. After the relaxation, $\gamma(\boldsymbol{x})$ and $\phi(\boldsymbol{x})$ at each phase transformation unit position ($\boldsymbol{x}$) were calculated using Eqs. (7) and (8), and $L_{11}^{II}(0, 0)(L_{33}^{II}(0, 0))$ was calculated using Eq. (10).

For the $L_{12}^{II}(L_{13}^{II})$ calculation, as in Fig. 7, planar supercell $\Omega_{12}^{twin}(\Omega_{13}^{twin})$ with 12 phase transformation units along both $\boldsymbol{x_1}$ and $\boldsymbol{x_2}$ ($\boldsymbol{x_1}$ and $\boldsymbol{x_3}$) -directions containing 576 atoms was prepared, and 6×6 twin units were embedded in the original (parent) structure. $L_{13}^{II} = L_{23}^{II}$ because BP and PB boundaries are crystallographically equivalent. Then, molecular statics ionic structure relaxation under zero stress conditions was carried out to obtain $G_{AS}^{12}(0, 0)(G_{AS}^{13}(0, 0))$. After relaxation, again, we calculated $\gamma(\boldsymbol{x})$ and $\phi(\boldsymbol{x})$, and $L_{12}^{II}(0, 0)(L_{13}^{II}(0, 0))$ was calculated using Eq. (11). In our DFT calculations, because of the cost of calculating G_{AS}^{ij}, we did not consider the temperature effects; thus, our free energy was obtained at the zero temperature limit without entropy and stress effects in L_{ij}^{II}; $L_{ij}^{II}(0, \boldsymbol{\sigma}^{ex}) \approx L_{ij}^{II}(0, 0)$ throughout the whole phase-field simulation.

Concerning the DFT calculations, we employed the Vienna *ab-initio* simulation package (VASP) [61] using the Perdew–Wang generalized gradient approximation functional [62] and projector-augmented wave potentials [63] for Mg ($3s^2 3p^0$ valence). An energy cutoff of 265 eV was used for the plane wave expansion. The energy convergence criteria of the electronic and ionic structure relaxations were set to 1.0×10^{-9} and 1.0×10^{-3} eV, respectively. For the electronic structure relaxation, the residual minimization scheme–direct inversion in the iterative subspace (RMM-DIIS) algorithm [64] was used. The computed HCP lattice parameters are $a_0/c_0 = 1.628$ and $a_0 = 0.319$ nm, and the shear modulus G for the twinning shear mode is 19.5 GPa. These values are consistent with those obtained in other theoretical studies ($a_0/c_0 = 1.628$ [65,66], $a_0 = 0.313$ nm [65] and $G = 21.49$ GPa [67]) and experimental measurements($a_0/c_0 = 1.624$ [46], $a_0 = 0.321$ nm [46] and $G = 19.37$ GPa [68]). The subroutines for independent stress and the strain component control [69] and atomic and supercell shape relaxation under constraints (drag method [70]) were implemented in the VASP code.

In Figs. 8–10, we show the calculated $\tilde{g}_{int}(\gamma, \phi)$ maps at 0, 1, 2, and 3 GPa twinning shear stresses ($\{10\bar{1}2\}\langle\bar{1}011\rangle$ shear stress) and the γ and ϕ distribution of the Ω_{ij}^{twin} supercell. In the $\tilde{g}_{int}(\gamma, \phi)$ map (Fig. 8), the red circles represent the stable (γ, ϕ) position before the twinning, it is the potential energy valley in $\gamma - \phi$ potential energy surface, under each shear stress condition. We can see the stable position shifts to positive γ direction though ϕ is remaining at zero as shear stress

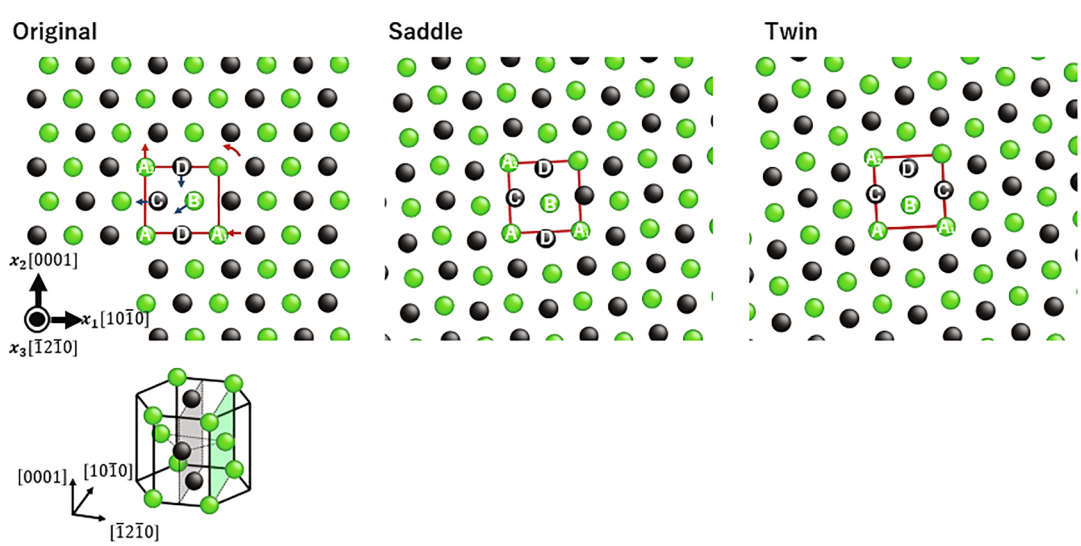

Fig. 5. Atomic structure change during the uniform $\{10\bar{1}2\}$ twinning deformation process. The red frame describes the phase transformation unit of the $\{10\bar{1}2\}$ twinning deformation. Red arrows indicate the cell shape change (lattice distortion) and rotation. Blue arrows indicate internal atomic displacement (shuffling). The different colored atoms represent atoms in each of the $(\bar{1}2\bar{1}0)$ atomic planes. (For interpretation of the references to colour in this figure legend, the reader is referred to the web version of this article.)

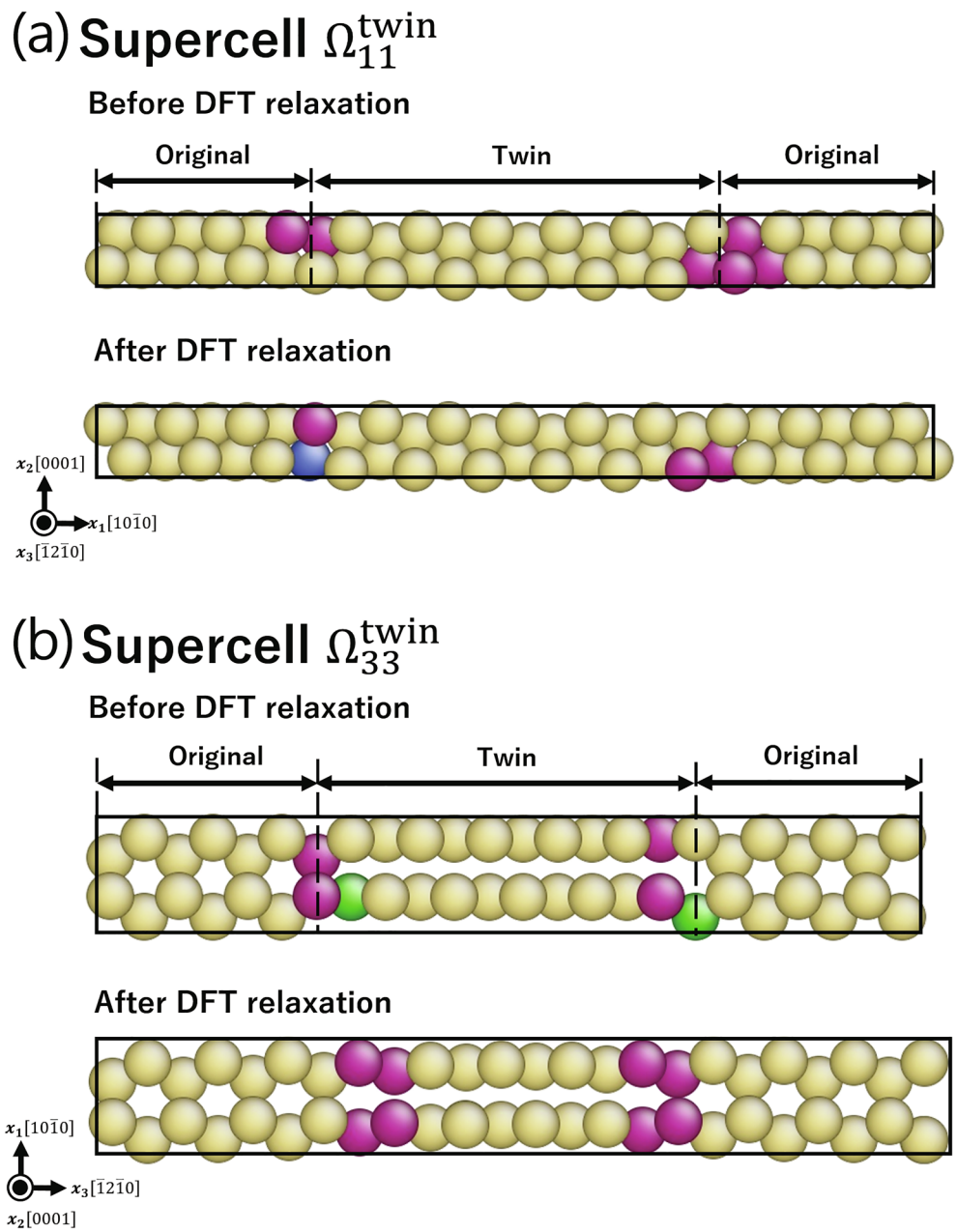

Fig. 6. Atomic structure of supercell (a) Ω_{11}^{twin} and (b) Ω_{33}^{twin} before and after DFT structural relaxation. The atomic structure is shown with coordination number coloring prepared using AtomEye [60]. The black frame represents the periodic boundary. (For interpretation of the references to colour in this figure legend, the reader is referred to the web version of this article.)

increase. This indicates internal atomic coordinate is not changed (shuffling does not occur) but the lattice is distorted by the shear stress. In the conventional phase-field method, linear relationship between γ and ϕ is assumed; $\gamma = \phi$ is conventional form and the stable position is always $\gamma = \phi = 0$ (or $\gamma = \phi = 1$) [33]. From Fig. 8, this assumption does not work once shear stress is applied. As a result, we cannot describe the correct pathway and the activation energy of the phase transformation and the quantitative energetics of phase transformation cannot be discussed using conventional phase-field method. In this sense, for the reliable energetic analysis using phase-field method, the potential energy surface in (γ, ϕ) space must be clarified based on reliable physical background of atomistic simulation and be informed to phase-field method. As shown by the γ and ϕ distribution in Fig. 9, γ distribution is almost uniform around $\gamma = 0.5$ in the Ω_{ii}^{twin} supercell, although the ϕ distribution is changing as we can distinguish with original and twinning region in atomic structure. On the other hand, in the $\Omega_{ij}^{twin}(i \neq j)$ supercell (Fig. 10), although ϕ is distributed to reflect the atomic structure in both (a) Ω_{12}^{twin} and (b) Ω_{13}^{twin} supercells, γ is almost zero in both (a) Ω_{12}^{twin} and (b) Ω_{13}^{twin} supercells. Thus, we can see the γ distribution differs depending on the atomic model. Because the elastic interaction is a long-range interaction, this difference is likely caused by the size limitation of atomic model, that is, the boundary effect of the atomic model [71,72]. In this sense, the elimination of the elastic effects from the atomistic free energy using Eqs. (10) and (11), which is equal to removing the size effect of the atomic model, is important for accurate phase-field modeling. By $\int_{\Omega_{ij}} g_{elast} dx$ term in Eqs. (10) and (11), which is calculated using micromechanics, the elastic interaction due to size limitation of atomistic simulation is fully eliminated. Similarly, because of the presence of a γ distribution in atomic model, the elastic energy is always double-counted when using the atomistically based free energy (G_{AS}) as the phase-field interfacial parameter *directly* together with micromechanics elastic energy. Finally, from the γ-ϕ

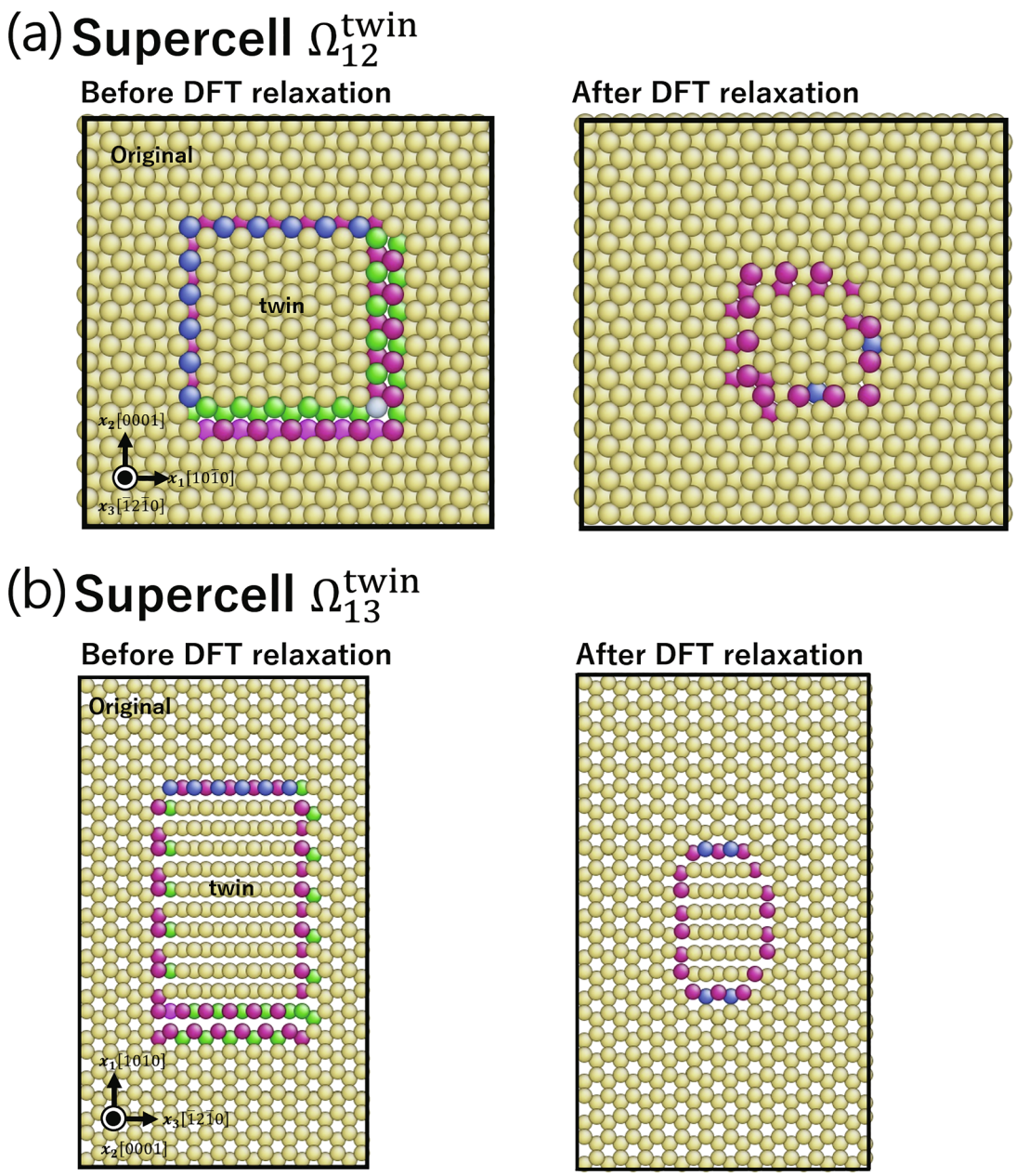

Fig. 7. Atomic structure of supercell (a) Ω_{12}^{twin} and (b) Ω_{13}^{twin} before and after DFT structural relaxation. The atomic structure is shown with coordination number coloring prepared using AtomEye [60]. The black frame represents the periodic boundary. (For interpretation of the references to colour in this figure legend, the reader is referred to the web version of this article.)

distribution and total free energy G_{AS}^{ij}, we derived $L_{11}^{II} = L_{22}^{II} = 2.94$, $L_{33}^{II} = 2.29$, $L_{12}^{II} = 1.20$ and $L_{13}^{II} = L_{23}^{II} = -0.09$ eV/nm for the following phase-field model.

3.3. Energetics of heterogeneous {10$\bar{1}$2} twin migration

In this study, we combined our atomistic informed phase-field model with the nudged elastic band method (NEB) [70] (PF-NEB) to determine the activation energy of heterogeneous {10$\bar{1}$2} twin migration. For convenience in the NEB calculations, we defined a 2 M-dimensional force vector $F \equiv \{f(x_1),\ f(x_2),\ \ldots,\ f(x_i),\ \ldots,\ f(x_M)\}$ and order parameter vector $\mathbf{\Phi} \equiv \{\gamma(x_1),\ \phi(x_1),\ \gamma(x_2),\ \phi(x_2),\ \ldots,\ \gamma(x_i),\ \phi(x_i),\ \ldots,\ \gamma(x_M),\ \phi(x_M)\}$ for the whole system. Here, M is total number of phase-field units in the system and $f \equiv \left\{-\frac{\partial G}{\partial \gamma}, -\frac{\partial G}{\partial \phi}\right\}$.

The force vector of the Ith image F_{neb}^{I} of the PF-NEB calculation is described as

$$F_{neb}^{I} = \begin{cases} F^{I} - \frac{\mathbf{\Phi}^{I+1} - \mathbf{\Phi}^{I-1}}{\|\mathbf{\Phi}^{I+1} - \mathbf{\Phi}^{I-1}\|}\left(F^{I}.\frac{\mathbf{\Phi}^{I+1} - \mathbf{\Phi}^{I-1}}{\|\mathbf{\Phi}^{I+1} - \mathbf{\Phi}^{I-1}\|}\right) + k(\mathbf{\Phi}^{I+1} - 2\mathbf{\Phi}^{I} + \mathbf{\Phi}^{I-1}) & 0 < I < L-1 \\ 0 & (I = 0 \ or \ L-1). \end{cases} \tag{12}$$

Here, k is spring constant. The free energy change ΔG^{I} from the initial state ($I = 0$) is described as a path integration in this study,

$$\Delta G^{I} = -\sum_{i=0}^{I-1} \frac{(F^{i+1} + F^{i})}{2}.(\mathbf{\Phi}^{i+1} - \mathbf{\Phi}^{i})(0 < I \leqslant L-1). \tag{13}$$

Concerning the detailed phase-field model, as the initial model, we created a supercell containing 101 × 101 × 51 units and distributed the order parameter $\gamma^{I}(x_1, x_2, x_3)$, $\phi^{I}(x_1, x_2, x_3)$ of image I using Eq. (14) like Fig. 11.

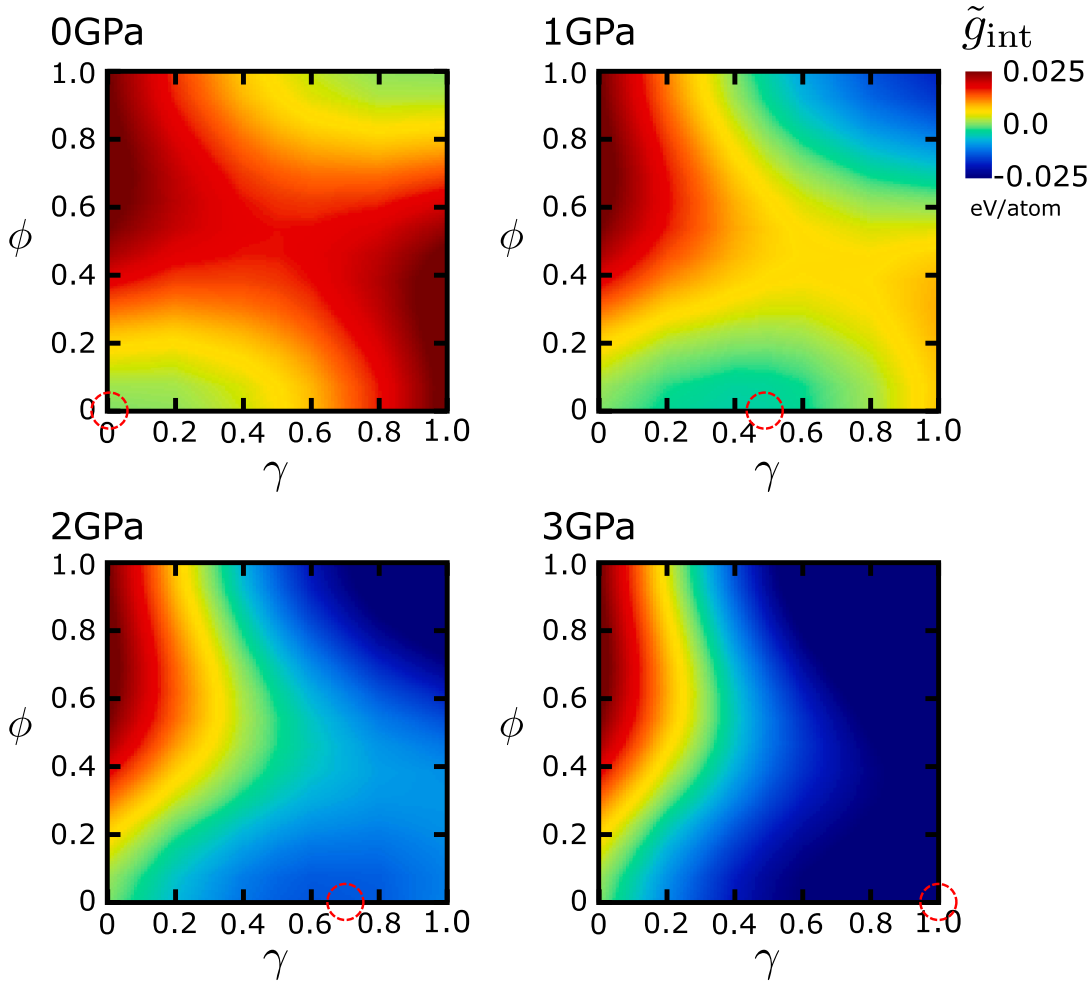

Fig. 8. $\tilde{g}_{\mathrm{int}}(\gamma, \phi)$ map of $\{10\bar{1}2\}$ deformation twinning at 0, 1, 2, and 3 GPa $\{10\bar{1}2\}\langle\bar{1}011\rangle$ shear stress. The red circles represent the stable (γ, ϕ) position before the twinning, the potential energy valley in $\gamma - \phi$ potential energy surface, under each shear stress condition. (For interpretation of the references to colour in this figure legend, the reader is referred to the web version of this article.)

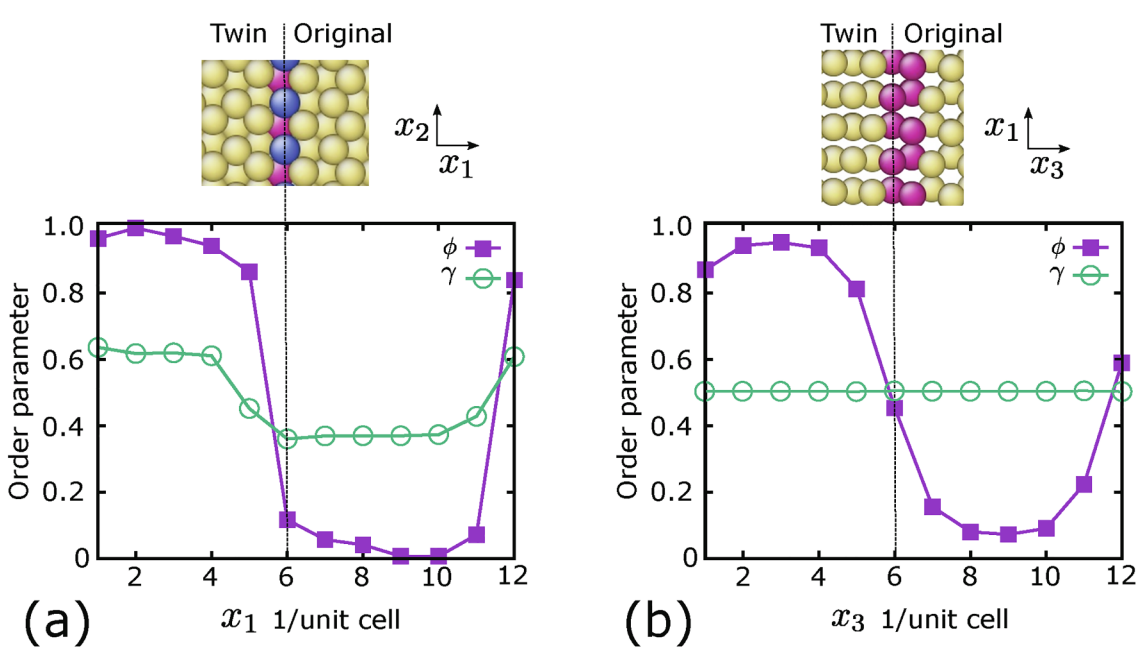

Fig. 9. γ and ϕ distributions of (a) $\Omega_{11}^{\mathrm{twin}}$ and (b) $\Omega_{33}^{\mathrm{twin}}$ supercells for the L_{ii}^{II} calculation. The atomic structure near the interface is shown with coordination number coloring prepared using AtomEye [60]. (For interpretation of the references to colour in this figure legend, the reader is referred to the web version of this article.)

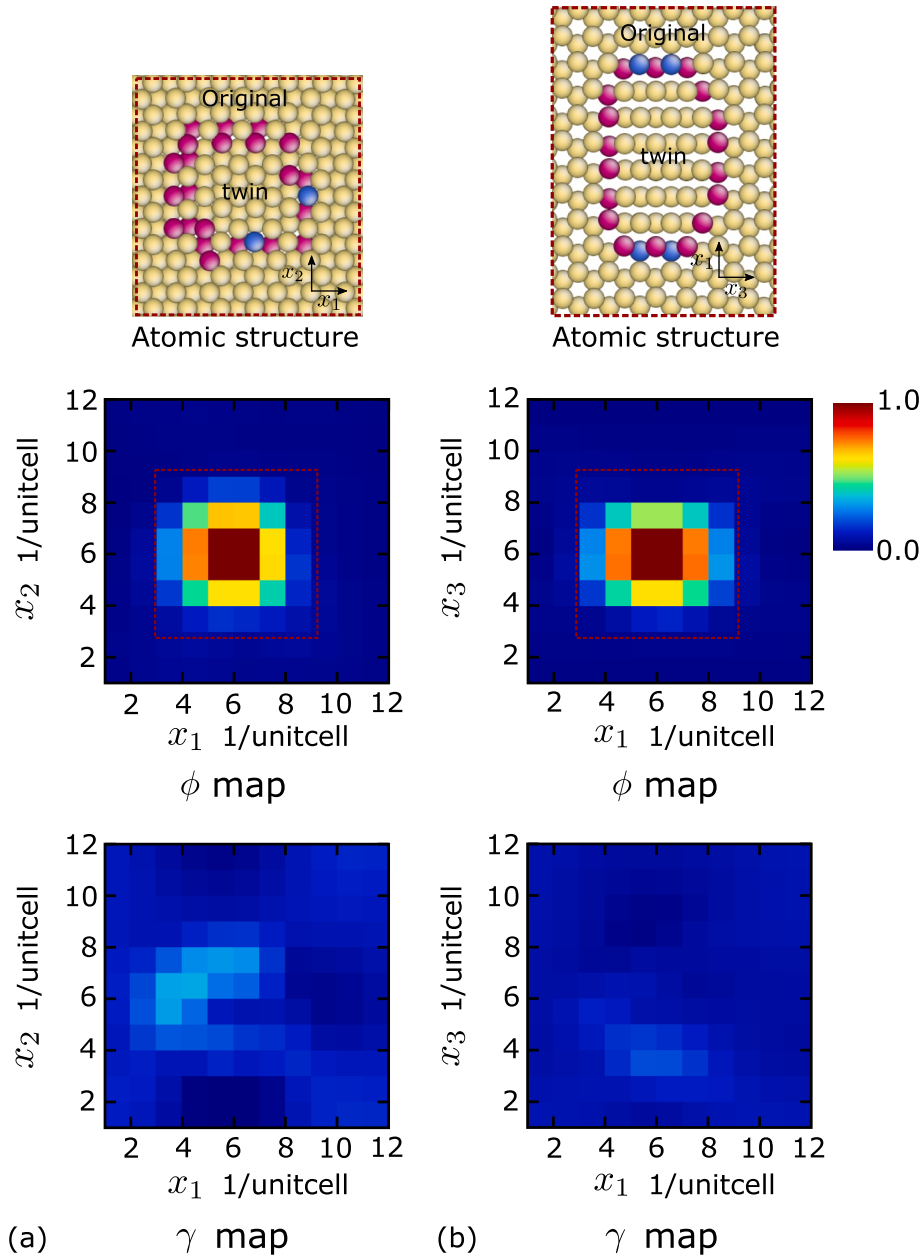

Fig. 10. γ and ϕ distributions of (a) $\Omega_{12}^{\text{twin}}$ and (b) $\Omega_{13}^{\text{twin}}$ supercells for $L_{ij}^{\text{II}}(i \neq j)$ calculation. The atomic structure around the embedded twin region (inside the red frame) is shown with coordination number coloring prepared using AtomEye [60]. (For interpretation of the references to colour in this figure legend, the reader is referred to the web version of this article.)

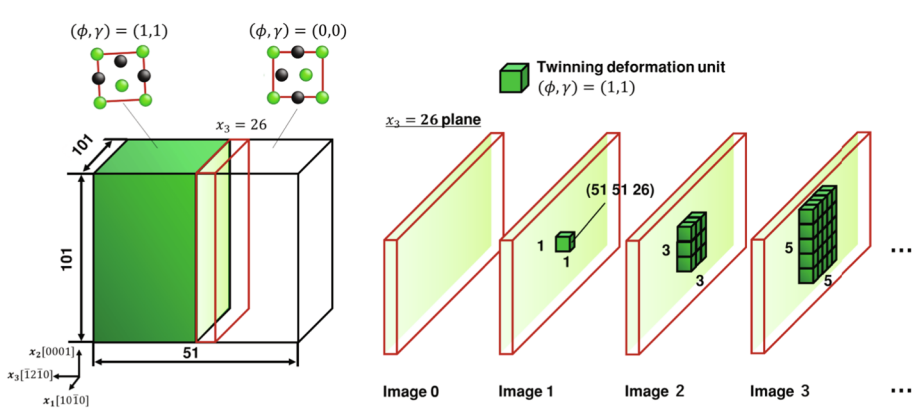

Fig. 11. Initial supercell for the PF-NEB calculations.

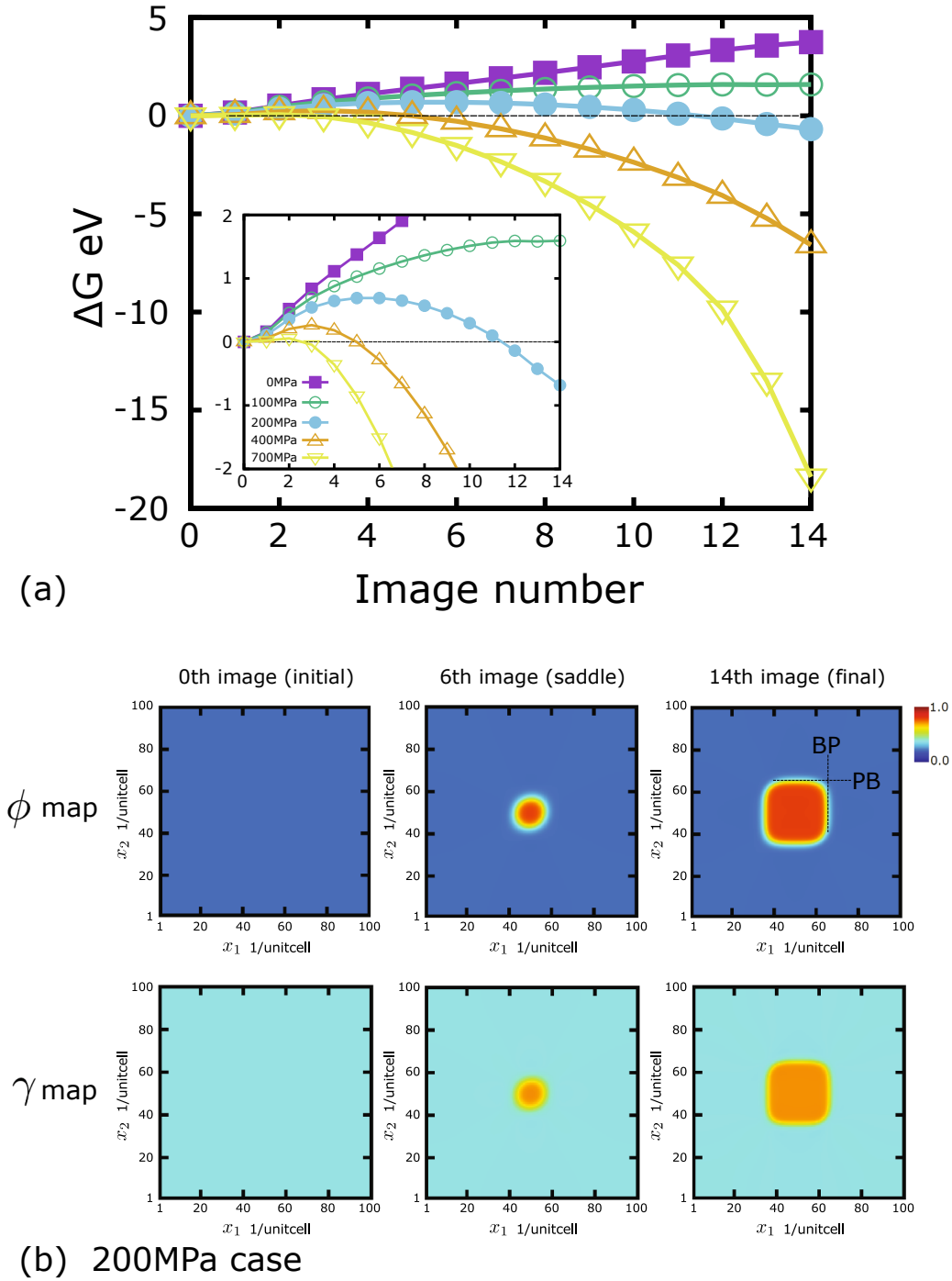

Fig. 12. (a) The free energy change (ΔG) during heterogeneous twin migration on the $x_3 = 26$ plane under 0, 100, 200, 400, and 700 MPa [0001] (x_2)-direction tensile stress condition. (b) γ and ϕ distribution of initial, saddle, and final states on the $x_3 = 26$ plane under 200 MPa [0001] tensile stress.

$$\gamma^I(x_1, x_2, x_3) = \phi^I(x_1, x_2, x_3) = \begin{cases} 1 & (x_3 < 26) \\ 1 & (51 - i \leqslant x_1 \leqslant 51 + i,\ 51 - i \leqslant x_2 \leqslant \\ & \quad 51 + i,\ x_3 = 26,\ 0 \leqslant i < I) \\ 0 & (otherwise). \end{cases} \tag{14}$$

As in Fig. 11, this model includes twinning and the original HCP region half and half along x_3-direction, and the gradual heterogeneous twinning evolution at the interface region ($x_3 = 26$ plane) is expressed as the increase of twinning region at the interface region with the increase of the NEB image number. Note this model corresponds to the atomic supercell with 2 million atoms. At present, it is impossible to analyze such large atomic model using DFT potential atomic simulation even with supercomputers. Concerning the PF-NEB settings, we set the total image number as $L = 15$, spring constant as $k = 0.1$, and timestep as $\Delta t = 0.05$. The energy convergence criteria was set to 1.0×10^{-3}eV, respectively. External tensile stress 0, 100, 200, 400, and 700 MPa along c-axis, [0001](x_2)-direction, is applied during PF-NEB simulation, corresponding 0.5 Schmid factor for $\{10\bar{1}2\}$ deformation twinning. Before the NEB calculations, the initial ($I = 0$) and final ($I = 14$) state structures were relaxed using our original phase-field scheme with same energy convergence criteria. The elastic constant for micromechanics is derived from our DFT calculations and is consistent with the results of previous studies [69].

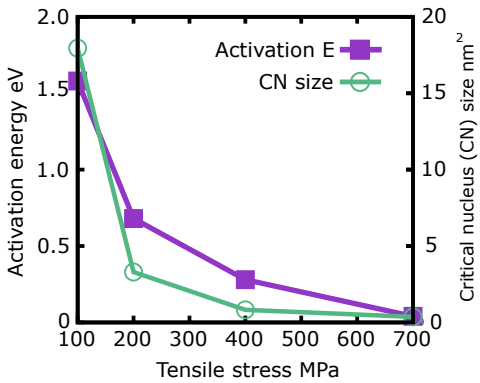

Fig. 13. [0001] tensile stress vs. activation energy and critical nucleus size of heterogeneous $\{10\bar{1}2\}$ twin migration.

In Fig. 12, we show (a) the free energy change ΔG during the heterogeneous $\{10\bar{1}2\}$ twin migration on the $x_3 = 26$ plane under 0, 100, 200, 400, and 700 MPa [0001] (x_2)-direction tensile stress conditions and (b) the γ and ϕ distributions of the initial, saddle, and final states under 200 MPa [0001] tensile stress on the $x_3 = 26$ plane, which were calculated using PF-NEB simulations. As shown in Fig. 12 (a), although there is no saddle point for twin migration at 0 MPa, a saddle point appears if we apply tensile stress, and the activation energy (ΔG at the saddle point) decreases as the stress increases. Eventually, the activation energy becomes almost zero at 700 MPa stress, and the critical tensile stress is 700 MPa for $\{10\bar{1}2\}$ twin migration at zero temperature. This is consistent with Qian *et al.*'s experimental yield stress of the $\{10\bar{1}2\}$ twinning deformation of HCP Mg nanopillar tensile tests [73]. Because the athermal stress of twinning migration is determined by the free energy change during that, we think this consistence is an evidence of the accurate energetics of our phase-field model. Because Mg HCP $\{10\bar{1}2\}$ deformation twinning is a lattice distortion and shuffling mixed phase transformation, this indicates the accurate correlation between lattice distortion and shuffling modes in the free energy surface from DFT potential is introduced to our phase-field model well.

As shown in Fig. 12(b), γ and ϕ change simultaneously during twin migration, and, in the initial state, $\gamma \approx 0.5$ and $\phi \approx 0.2$ over the whole $x_3 = 26$ plane. The initial state γ and ϕ distributions are consistent with the ϕ and γ distributions in Fig. 9(b)$x_3 = 7$) DFT result, confirming the validity of our phase-field code; DFT atomic lattice distortion and shuffling behaviors are well reproduced. Further, during the twinning migration, we found isotropic twin embrio appears and grows with BP and PB boundaries. Because BP and PB boundaries are crystallographically equivalent; both interfacial energies are same, we think this symmetric nucleation is reasonable. The nucleation of Mg $\{10\bar{1}2\}$ deformation twin with BP and PB boundaries are also reported in experiment [74,75]. This is due to the low interface energy of BP and PB boundaries [55].

In Fig. 13, we show the [0001] tensile stress vs. activation energy and critical nucleus of heterogeneous $\{10\bar{1}2\}$ twin migration. The critical nucleus size was estimated from the ϕ distribution map at the saddle point under each stress condition;we consider $\{x \mid \phi(x) > 0.5\}$ as twin region. The nucleus size of $\{10\bar{1}2\}$ twin migration is nanometer-sized under stress of hundred megapascals. Although the heterogeneous nucleation of grains, which form polycrystal including twinning region, from *liquids* can be observed by large-scale molecular dynamics [76], the heterogeneous nucleation of deformation twinning from the *original lattice structure* and critical nucleus size of that are still unclear at present because the chemical potential energy is not changed by twinning deformation (i.e., the original lattice structure and twinning structure are crystallographically equivalent) and the estimated critical nucleus size by classical nucleation theory is very large, i.e., micrometers [77]. Thus, this is the first reasonable result for the critical nucleus size of deformation twinning if we remember that nanotwinning is always observed in nanopolycrystalline materials [78,79].

Note our previous research suggests that shuffling is dominant for the $\{10\bar{1}2\}$ deformation twinning [27], meaning temperature effects and vibrational entropy may be important factors in $\{10\bar{1}2\}$ deformation twinning [27]. Because of the high cost of DFT calculations, we cannot include temperature effects for this phase-field $\{10\bar{1}2\}$ twin migration analysis at present. However, in future work, we plan to include temperature effects in our phase-field model of $\{10\bar{1}2\}$ deformation twinning using empirical potentials, which can express the properties of $\{10\bar{1}2\}$ twinning deformation well.

4. Summary

In summary, we have constructed an atomistically based phase-field model for the quantitative energetic analysis of phase transformations. To describe the general phase transformation with non-linear correlation between displacive and diffusive modes, we defined two order parameters, γ and ϕ, which describe the lattice distortion (displacive mode) and shuffling (diffusive mode), respectively. In addition, we have provided a way to introduce the energetics from atomistic simulations to the phase-field model: a description of γ and ϕ in the atomic model and a way to derive the phase-field parameters from the free energy calculated from atomistic simulations. Our phase-field model is applicable to the conventional solid–solid phase transformation with atomic shuffling component during phase transformation, e.g., twinning deformation in HCP metals [30], $\alpha - \omega$ martensite transformation in titanium [80] and FCC to BCT martensite transformation in steel [81].To test the applications of our method, we used the free energy obtained using molecular statics calculations with a DFT potential to calculate the free energy change during heterogeneous $\{10\bar{1}2\}$ twin migration of HCP Mg and the activation energy and critical nucleus size of the heterogeneous $\{10\bar{1}2\}$ twin migration under certain stress conditions by combining our phase-field model with the NEB method. The critical *c*-axis tensile stress (athermal stress) at which the activation energy goes to zero agrees well with the experimental yield stress of $\{10\bar{1}2\}$ for the twinning deformation of HCP Mg nanopillar tensile tests. The critical nucleus size of the heterogeneous $\{10\bar{1}2\}$ twin migration is nanometer-sized under stresses of hundreds of megapascals, which is reasonably consistent with the experimental observation of nanotwins.

CRediT authorship contribution statement

Akio Ishii: Conceptualization, Methodology, Software, Validation, Investigation, Writing - original draft, Writing - review & editing, Visualization, Funding acquisition.

Declaration of Competing Interest

The authors declare that they have no known competing financial interests or personal relationships that could have appeared to influence the work reported in this paper.

Acknowledgements

This study was partially supported by a Grant-in-Aid for Early Career Scientists, 18K13658. DFT calculations were partly carried out through the use of OCTOPUS large-scale computer systems at the Cybermedia Center, Osaka University. A.I. thanks Prof. Shigenobu Ogata for many helpful discussions.

References

[1] L. Chen, Phase-field models for microstructure evolution, Ann. Rev. Mater. Res. 32 (2002) 113–140.
[2] Y. Wang, J. Li, Phase field modeling of defects and deformation, Acta Mater. 58

(2010) 1212–1235.
[3] D. Wang, Q. Liang, S. Zhao, P. Zhao, T. Zhang, L. Cui, Y. Wang, Phase field simulation of martensitic transformation in pre-strained nanocomposite shape memory alloys, Acta Mater. 164 (2019) 99–109.
[4] R. Shi, Y. Zheng, R. Banerjee, H.L. Fraser, Y. Wang, ω-Assisted α nucleation in a metastable β titanium alloy, Scr. Mater. 171 (2019) 62–66.
[5] A. Yamanaka, K. McReynolds, P.W. Voorhees, Phase field crystal simulation of grain boundary motion, grain rotation and dislocation reactions in a BCC bicrystal, Acta Mater. 133 (2017) 160–171.
[6] C. Shen, J. Li, Y. Wang, Predicting structure and energy of dislocations and grain boundaries, Acta Mater. 74 (2014) 125–131.
[7] D. Qiu, P. Zhao, C. Shen, W. Lu, D. Zhang, M. Mrovec, Y. Wang, Predicting grain boundary structure and energy in BCC metals by integrated atomistic and phase-field modeling, Acta Mater. 164 (2019) 799–809.
[8] T. Takaki, T. Shimokawabe, M. Ohno, A. Yamanaka, T. Aoki, Unexpected selection of growing dendrites by very-large-scale phase-field simulation, J. Crys. Grow. 382 (2013) 21–25.
[9] T. Takaki, Phase-field modeling and simulations of dendrite growth, ISIJ Int. 54 (2014) 437–444.
[10] H. Neumann-Heyme, K. Eckert, C. Beckermann, Dendrite fragmentation in alloy solidification due to sidearm pinch-off, Phys. Rev. E 92 (2015) 060401 .
[11] T. Aoki, T. Takaki, Y. Shibuta, M. Ohno, S. Sakane, Permeability prediction for flow normal to columnar solidification structures by large scale simulations of phase field and lattice Boltzmann methods, Acta Mater. 164 (2019) 237–249.
[12] G. Kim, T. Takaki, Y. Shibuta, S. Sakane, K. Matsuura, M. Ohno, A parametric study of morphology selection in equiaxed dendritic solidification, Comput. Mater. Sci. 162 (2019) 76–81.
[13] E. Miyoshi, T. Takaki, M. Ohno, Y. Shibuta, S. Sakane, T. Shimokawabe, T. Aoki, Ultra-large-scale phase-field simulation study of ideal grain growth, NPJ Comp. Mater. 3 (2017) 1–5.
[14] Q. Peng, Y.J. He, Z. Moumni, A phase-field model on the hysteretic magneto-mechanical behaviors of ferromagnetic shape memory alloy, Acta Mater. 88 (2015) 13–24.
[15] A. Vidyasagar, W.L. Tan, D.M. Kochmann, Predicting the effective response of bulk polycrystalline ferroelectric ceramics via improved spectral phase field methods, J. Mech. Phys. Sol. 106 (2017) 133–151.
[16] Y. Cui, N. Hatcher, Y. Gao, F. Yang, N. Zhou, L. Kovarik, R. Noebe, M. Mills, Y. Wang, P-phase precipitation and its effect on martensitic transformation in (Ni, Pt)Ti shape memory alloys, Acta Mater. 60 (2012) 1514–1527.
[17] H. Song, R. Shi, Y. Wang, J.J. Hoyt, Simulation study of heterogeneous nucleation at grain boundaries during the austenite-ferrite phase transformation: comparing the classical model with the multi-phase field nudged elastic band method, Metall. Mater. Trans. A 48 (2017) 2730–2738.
[18] J.R. Mianroodi, B. Svendsen, Atomistically determined phase-field modeling of dislocation dissociation, stacking fault formation, dislocation slip, and reactions in fcc systems, J. Mech. Phys. Sol. 77 (2015) 109–122.
[19] Z.G. Mei, L. Liang, Y.S. Kim, T. Wiencek, E. O'Hare, A.M. Yacout, G. Hofman, M. Anitescu, Grain growth in U-7Mo alloy: A combined first-principles and phase field study, J. Nucl. Mater. 473 (2016) 300–308.
[20] J.R. Mianroodi, P. Shanthraj, P. Kontis, J. Cormier, B. Gault, B. Svendsen, D. Raabe, Atomistic phase field chemomechanical modeling of dislocation-solute-precipitate interaction in Ni-Al-Co, Acta Mater. 175 (2019) 250–261.
[21] D.E. Spearot, V. Taupin, K. Dang, L. Capolungo, Mechanics of Materials Structure and kinetics of three-dimensional defects on the $\{10\bar{1}2\}$ boundary in magnesium: Atomistic and phase-field simulations, Mech. Mater. 143 (2020) 103314 .
[22] C. Liu, P. Shanthraj, J.D. Robson, M. Diehl, S. Dong, J. Dong, W. Ding, D. Raabe, On the interaction of precipitates and tensile twins in magnesium alloys, Acta Mater. 178 (2019) 146–162.
[23] E. Miyoshi, T. Takaki, Y. Shibuta, M. Ohno, Bridging molecular dynamics and phase-field methods for grain growth prediction, Comp. Mater. Sci. 152 (2018) 118–124.
[24] O. Shchyglo, T. Hammerschmidt, M. Čak, R. Drautz, I. Steinbach, Atomistically informed extended Gibbs energy description for phase-field simulation of tempering of martensitic steel, Materials 9 (2016) 1–9.
[25] S. Kavousi, B.R. Novak, M.A. Zaeem, D. Moldovan, Combined molecular dynamics and phase field simulation investigations of crystal-melt interfacial properties and dendritic solidification of highly undercooled titanium, Comput. Mater. Sci. 163 (2019) 218–229.
[26] J.W. Christian, The Theory of Transformations in Metals and Alloys, Pergamon, Oxford, 2002.
[27] A. Ishii, J. Li, S. Ogata, Shuffling-controlled versus strain-controlled deformation twinning: The case for HCP Mg twin nucleation, Inter. J. Plas. 82 (2016) 32–43.
[28] P. Cao, M.P. Short, S. Yip, Understanding the mechanisms of amorphous creep through molecular simulation, Proc. Nat. Aca. Sci. 114 (2017) 13631–13636.
[29] T. Ezaz, H. Sehitoglu, Coupled shear and shuffle modes during twin growth in B2-NiTi, Appl. Phys. Lett. 98 (2011) 241906 .
[30] H. El Kadiri, C.D. Barrett, M.A. Tschopp, The candidacy of shuffle and shear during compound twinning in hexagonal close-packed structures, Acta Mater. 61 (2013) 7646–7659.
[31] A.S.K. Mohammed, H. Sehitoglu, Modeling the interface structure of type II twin boundary in B19' NiTi from an atomistic and topological standpoint, Acta Mater. 183 (2020) 93–109.
[32] A.S.K. Mohammed, H. Sehitoglu, Martensitic twin boundary migration as a source of irreversible slip in shape memory alloys, Acta Mater. 186 (2020) 50–67.
[33] P. Zhao, C. Shen, J. Li, Y. Wang, Effect of nonlinear and noncollinear transformation strain pathways in phase-field modeling of nucleation and growth during martensite transformation, npj Comp, Mater. 3 (2017) 1–10.
[34] H. Babaei, V.I. Levitas, Phase-field approach for stress- and temperature-induced phase transformations that satisfies lattice instability conditions. Part 2. Simulations of phase transformations Si I → Si II, Int. J. Plas. 107 (2018) 223–245.
[35] V.I. Levitas, Phase field approach for stress- and temperature-induced phase transformations that satisfies lattice instability conditions. Part I. General theory, Int. J. Plas. 106 (2018) 164–185.
[36] H. Babaei, V.I. Levitas, Effect of 60° dislocation on transformation stresses, nucleation, and growth for phase transformations between silicon I and silicon II under triaxial loading: Phase-field study, Acta Mater. 177 (2019) 178–186.
[37] B. Xu, G. Kang, Q. Kan, C. Yu, X. Xie, Phase field simulation on the cyclic degeneration of one-way shape memory effect of NiTi shape memory alloy single crystal, Inter. J. Mech. Sci. 168 (2020) 105303 .
[38] X.-Z. Tang, Q. Zu, Y.-F. Guo, The diffusive character of extension twin boundary migration in magnesium, Materialia 2 (2018) 208–213.
[39] J.W. Cahn, J.E. Hilliard, Free energy of a nonuniform system. I. Interfacial free energy, J. Chem. Phys. 28 (1958) 258–267.
[40] I. Steinbach, F. Pezzolla, A generalized field method for multiphase transformations using interface fields, Physica D: Nonlinear Phenomena 134 (1999) 385–393.
[41] L.Q. Chen, W. Yang, Computer simulation of the domain dynamics of a quenched system with a large number of nonconserved order parameters: The grain-growth kinetics, Phys. Rev. B 50 (1994) 15752–15756.
[42] P. Zhao, J. Li, Y. Wang, Heterogeneously randomized STZ model of metallic glasses: Softening and extreme value statistics during deformation, Inter. J. Plas. 40 (2013) 1–22.
[43] P. Zhao, J. Li, Y. Wang, Extended defects, ideal strength and actual strengths of finite-sized metallic glasses, Acta Mater. 73 (2014) 149–166.
[44] T. Mura, Micromechanics of Defects in Solids, Springer Science & Business Media, 2013.
[45] J. Wang, J. Li, S. Yip, S. Phillpot, D. Wolf, Mechanical instabilities of homogeneous crystals, Phys. Rev. B 52 (1995) 12627–12635.
[46] M.H. Yoo, Slip, twinning, and fracture in hexagonal close-packed metals, Metall. Trans. A 12A (1981) 409–418.
[47] H. Yoshinaga, R. Horiuchi, On the nonbasal slip in magnesium crystals, Trans. J. Inst. Metals 5 (1963) 14–21.
[48] A. Chapuis, J.H. Driver, Temperature dependency of slip and twinning in plane strain compressed magnesium single crystals, Acta Mater. 59 (2011) 1986–1994.
[49] J. Wang, S.K. Yadav, J.P. Hirth, C.N. Tomé, I.J. Beyerlein, Pure-shuffle nucleation of deformation twins in hexagonal-close-packed metals, Mater. Res. Lett. 1 (2013) 126–132.
[50] A. Ostapovets, P. Molnár, On the relationship between the "shuffling-dominated" and "shear-dominated" mechanisms for twinning in magnesium, Scr. Mater. 69 (2013) 287–290.
[51] A. Ostapovets, R. Gröger, Twinning disconnections and basal-prismatic twin boundary in magnesium, Modell. Simu. Mater. Sci. Eng. 22 (2014) 025015 .
[52] C.D. Barrett, H. El Kadiri, Impact of deformation faceting on $\{10\bar{1}2\}$, $\{10\bar{1}1\}$ and $\{10\bar{1}3\}$ embryonic twin nucleation in hexagonal close-packed metals, Acta Mater. 70 (2014) 137–161.
[53] N. Zhou, G. Zhang, T.F. Guo, X. Guo, S. Tang, X. Huang, Twin nucleation at prismatic/basal boundary in hexagonal close-packed metals, Phil. Mag. 99 (2019) 2584–2603.
[54] G. Zhou, L. Ye, H. Wang, D. Xu, C. Meng, R. Yang, Energy paths of twin-related lattice reorientation in hexagonal metals via ab initio calculations, J. Mater. Sci. Tech. 34 (2017) 700–707.
[55] A. Kumar, J. Wang, C.N. Tomé, First-principles study of energy and atomic solubility of twinning-associated boundaries in hexagonal metals, Acta Mater. 85 (2015) 144–154.
[56] Z. Pei, X. Zhang, T. Hickel, M. Friák, S. Sandlöbes, B. Dutta, J. Neugebauer, Atomic structures of twin boundaries in hexagonal close-packed metallic crystals with particular focus on Mg, NPJ Comput. Mater. 3 (2017) 1–6.
[57] L. Leclercq, L. Capolungo, D. Rodney, Atomic-Scale Comparison Between $\{\bar{1}101\}$ and $\{\bar{1}102\}$ Twin Growth Mechanisms in Magnesium, Mater. Res. Lett. 2 (2014) 152–154.
[58] O. Mackain, M. Cottura, D. Rodney, E. Clouet, Atomic-scale modeling of twinning disconnections in zirconium, Phys. Rev. B 95 (2017) 134102 .
[59] B. Li, X. Zhang, Global strain generated by shuffling-dominated twinning, Scr. Mater. 71 (2014) 45–48.
[60] J. Li, AtomEye: An efficient atomistic configuration viewer, Modell. Simu. Mater. Sci. Eng. 11 (2003) 173–177.
[61] G. Kresse, J. Furthmüller, Efficient iterative schemes for ab initio total-energy calculations using a plane-wave basis set, Phys. Rev. B 54 (1996) 11169–11186.
[62] J.P. Perdew, J.A. Chevary, S.H. Vosko, Atoms, molecules, solids, and surfaces: Applications of the generalized gradient approximation for exchange and correlation, Phys. Rev. B 46 (1992) 6671–6687.
[63] G. Kresse, D. Joubert, From ultrasoft pseudopotentials to the projector augmented-wave method, Phys. Rev. B 59 (1999) 11–19.
[64] P. Pulay, Convergence acceleration of iterative sequences. The case of SCF iteration, Chem. Phys. Lett. 73 (1980) 393–398.
[65] Y. Nie, Y. Xie, Ab initio thermodynamics of the hcp metals Mg, Ti, and Zr, Phys. Rev. B 75 (2007) 174117 .
[66] S. Sandlöbes, M. Friák, S. Zaefferer, A. Dick, S. Yi, D. Letzig, Z. Pei, L.F. Zhu, J. Neugebauer, D. Raabe, The relation between ductility and stacking fault energies in Mg and Mg-Y alloys, Acta Mater. 60 (2012) 3011–3021.
[67] S. Ogata, J. Li, N. Hirosaki, Y. Shibutani, S. Yip, Ideal shear strain of metals and ceramics, Phys. Rev. B 70 (2004) 104104 .
[68] L.J. Slutsky, C.W. Garland, Elastic constants of magnesium from 4.2°K to 300°K,

Phys. Rev. 107 (1957) 972–976.
[69] S. Ogata, J. Li, S. Yip, Energy landscape of deformation twinning in bcc and fcc metals, Phys. Rev. B 71 (2005) 224102 .
[70] H. Jonsson, G. Mills, K.W. Jacobsen, Nudged elastic band method for finding minimum energy paths of transitions, in: B.J. Berne, G. Ciccotti, D.F. Coker (Eds.), Classical and Quantum Dynamics in Condensed Phase Simulations, World Scientific, Singapore, 1998.
[71] J.E. Sinclair, P.C. Gehlen, R.G. Hoagland, J.P. Hirth, Flexible boundary conditions and nonlinear geometric effects in atomic dislocation modeling, J. Appl. Phys. 49 (1978) 3890–3897.
[72] X. Li, Efficient boundary conditions for molecular statics models of solids, Phys. Rev. B 80 (2009) 104112 .
[73] Q. Yu, L. Qi, K. Chen, R.K. Mishra, J. Li, A.M. Minor, The nanostructured origin of deformation twinning, Nano lett. 12 (2012) 887–892.
[74] B. Liu, J. Wang, B. Li, L. Lu, X. Zhang, Z. Shan, J. Li, C. Jia, J. Sun, E. Ma, Twinning-like lattice reorientation without a crystallographic twinning plane, Nat. Commun. 5 (2014) 3297.
[75] B.M. Morrow, R.J. McCabe, E.K. Cerreta, C.N. Tomé, Observations of the atomic structure of tensile and compressive twin boundaries and twin-twin interactions in zirconium, Metall. Mater. Trans. A 45 (2014) 5891–5897.
[76] Y. Shibuta, S. Sakane, E. Miyoshi, S. Okita, T. Takaki, M. Ohno, Heterogeneity in homogeneous nucleation from billion-atom molecular dynamics simulation of solidification of pure metal, Nat. Commun. 8 (2017) 1–10.
[77] J.S. Koehler, F. Seitz, W.T. Read JR, W. Shockley, E. Orowan, Dislocations in Metals, AIME, New York, 1954.
[78] L. Lu, Y. Shen, X. Chen, L. Qian, K. Lu, Ultrahigh strength and high electrical conductivity in copper, Science 304 (2004) 422–426.
[79] X. Li, Y. Wei, L. Lu, K. Lu, H. Gao, Dislocation nucleation governed softening and maximum strength in nano-twinned metals, Nature 464 (2010) 877–880.
[80] D. Trinkle, R. Hennig, S. Srinivasan, D. Hatch, M. Jones, H. Stokes, R. Albers, J. Wilkins, New mechanism for the α to ω martensitic transformation in pure titanium, Phys. Rev. Lett. 91 (2003) 1–4 025701.
[81] X.S. Yang, S. Sun, H.H. Ruan, S.Q. Shi, T.Y. Zhang, Shear and shuffling accomplishing polymorphic fcc $\gamma\rightarrow$ hcp $\varepsilon\rightarrow$ bct α martensitic phase transformation, Acta Mater. 136 (2017) 347–354.